A study of solid rocket motor ignition overpressure waves: jet flow development and IR radiation

Jean-Baptiste Dargaud⋆ *and Julien Troyes*⋆⋆
Jean-Michel Lamet⋆⋆ *and Lionel Tessé*⋆⋆
François Vuillot⋆⋆
Christophe Bailly†
⋆ *PhD student, Onera and CNES*
⋆⋆ *Onera – The French Aerospace Lab*
F-92322 Châtillon, France
† *LMFA, Ecole Centrale de Lyon*

Abstract

Space vehicles undergo harsh acoustic fields during launch. In order to efficiently reduce the load transmitted to the pad and the launcher, it is necessary to understand and characterize the strong pressure waves that are emitted at Solid propellant Rocket Motor (SRM) start-up. This is one of the main concerns of the research group AEID (Acoustique et Environnement Induits au Décollage). AEID was created in 1990 to understand the noise radiation mechanisms associated with hot supersonic jets and to design noise reduction systems. It is composed by ASTRIUM, CEAT (University of Poitiers), CNES, ECL, PPRIME and Onera. Computational study of the waves observed during the firing of a model SRM is presented in this paper. The experimental set-up is a scale down model for the Ariane 5 P230 SRM, named LP10, fired horizontally. Sensors record pressure in the far field and in the combustion chamber while high speed infrared (IR) band III camera tapes signature of the jet near the nozzle exit. This paper presents 3D LES computations carried out with Onera CFD code Cedre of the IOP and the hot supersonic jet expansion. As combustion products may react with ambient air, reactive computations are performed using a reduced chemical kinetic scheme. IR images of the plume downstream the nozzle are computed with radiative heat transfer solver Astre included in Cedre at camera recording frequency. Results are detailed and compared with experimental data. A good agreement is found between the far field pressure signal of the IOP as well as radiative computations results and measurements.

1. Introduction

Strong pressure waves are emitted at Solid propellant Rocket Motor (SRM) ignition. In aerospace applications, these waves may turn to be dangerous for the launcher payload as they propagate from the launchpad. A insightful understanding of this phenomenon is required to design efficient wave reduction systems.
A study of the waves observed at the firing of a small scale test rocket is presented in this paper, and to that purpose, Onera Cedre (cedar tree in French) CFD code is used. This latter is a parallel multiphysics computational tool for numerical simulations in the field of energetics (with particular emphasis on propulsion application) developed and validated by Onera. Gas phase physics is solved using Charme [1] and radiative heat transfer is resolved with Astre [2, 3, 4]. The discrete geometrical model consists in a general polyhedral conforming mesh.
The study focuses on the start-up phase of a SRM during which is emitted the Ignition Over Pressure (IOP), driven by the high pressure rise rate [5] in the motor chamber. The experimental setup is a scaled down model for Ariane 5 P230 SRM, named LP10. This paper presents 3D LES computation of the full-scale model firing. Comparisons are made with measured pressure time signals as well as with infra-red images from a high speed camera.

2. Experimental set up and available measurements

The motor was fired horizontally 1 m above the ground into open space, with instrumentation featuring acoustical and visual records.

2.1 Motor geometry and propellant disposition

The engine front end encloses the igniter. A general view of the propellant arrangement inside the combustion chamber and the nozzle position is shown in Figure 1. The propellant is composed of 5% aluminium in mass, and is organized in cylindrical and conical segments. The hot gas produced during the propellant combustion are expulsed from the cylindrical combustion chamber through a submerged nozzle at rear end. The latter is characterized by the ratio between its exit area and its throat area $A_j/A^* = 7.5625$. The nozzle is closed with an aluminum seal designed to break under a given pressure (here ≈15 bar).

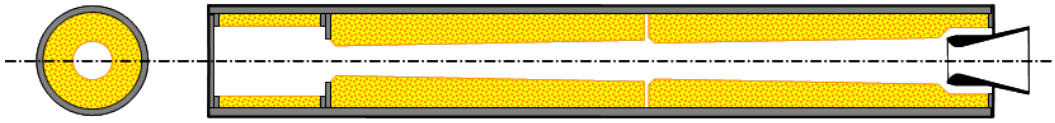

Figure 1: Model SRM geometry, propellant grain organization and nozzle disposition

2.2 Available measurements

During the test, the following records were made: pressure in the combustion chamber by high-frequency piezo electric transducers; IOP wave characteristics by far field microphones; images of the jet plume by visible and IR cameras. Figure 2 is a schematic top view of the experimental installation. The chamber pressure sensor (P_{far}) is located near

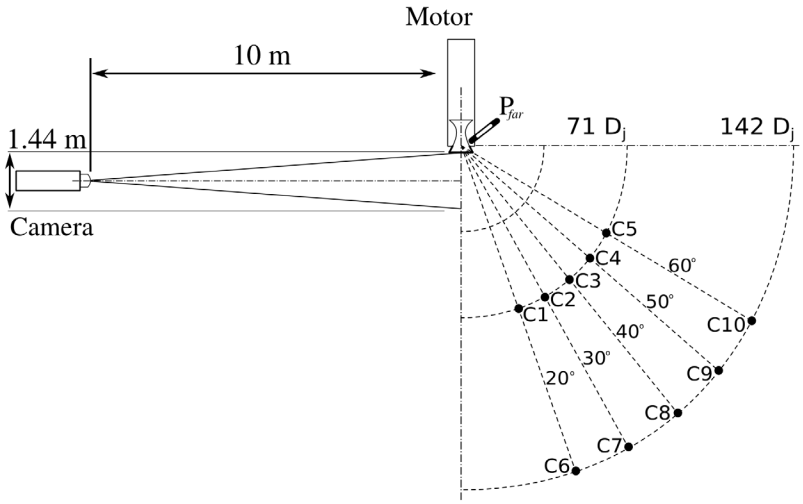

Figure 2: Chamber pressure sensor position, far field transducers location and video setup.

the nozzle, while the far field transducers are set up in two arcs, in an horizontal plane at nozzle center height. First arc is 71 D_j from nozzle throat and second is 142 D_j. Both spread from 20° to 60° on one side of the jet. Only the first five microphones will be used for comparison (C_1 to C_5). Finally, the infrared camera is disposed at 10 m from the plume centerline. It is equipped with a 25 mm lens that films an area extending from nozzle exit to l =1.44 m downstream with a height h =0.77 m, as displayed in Figure 2. An image is composed of 120 × 60 pixels, corresponding to a spatial resolution of 12 × 12.83 (mm×mm).
The jet plume is recorded every 0.5 ms in IR band III domain, which concerns radiative wavelengths from 8 to 9.3 μm and has been selected after examining imagery from other firings. The transmission curve of the optical filter is shown on Figure 3.

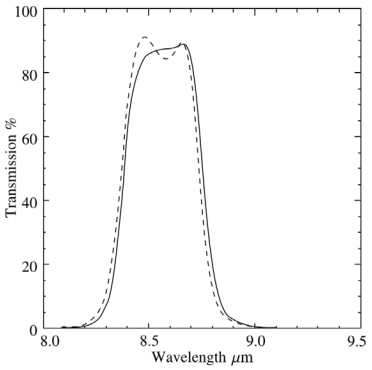

Figure 3: IR filter transmission as function of optical wavelength

2.3 Jet properties

Jet properties are governed by the combustion chamber pression. The properties at the nozzle exit plane are easily computed from isentropic relations, with $\gamma = 1.236$: the exit Mach number is M_j=3.17, and the total pressure over static pressure ratio at nozzle exit is $P_i/P_j = 60.14$.

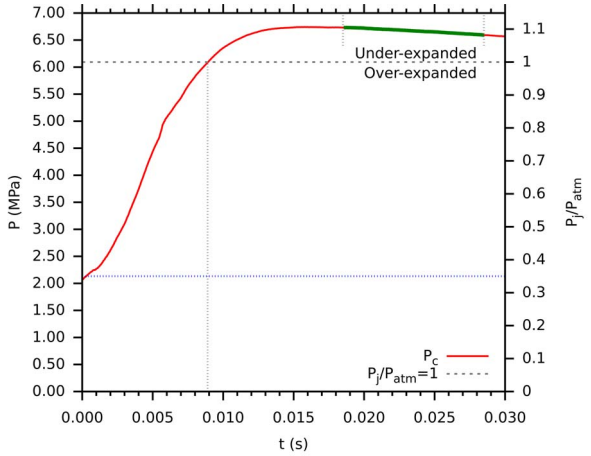

Figure 4: Time history of combustion chamber pressure. *Left scale:* detail of combustion chamber pressure ; *right scale:* nozzle exit static pressure over atmospheric pressure ratio

The IOP is a non-stationary phenomenon that occurs at ignition. and only the first 30 milliseconds after the seal break-up are of interest for what follows. The chamber pressure history is represented on Figure 4.
Morrisette [6] found experimentally that the flow separation criterion for conical nozzle operating at a designed Mach number of 3.17 is around P_j/P_{atm}=0.35 (blue dotted line in Figure 4). Thus, no flow separation is expected. Moreover, as the pressure of the jet flow at nozzle exit is not equal to ambient pressure, the jet is non adapted: a series of expansion fans and compression shocks is also expected.
The firing can be divided in two parts on the considered time period: the chamber pressure high rate (4.09 bar.ms^{-1}) rising until $\approx$ 15 ms and then a quasi-steady chamber pressure. By averaging pressure on a portion of this second phase (ranging over 10 ms and represented by the green line in Figure 4), it is possible to achieve a first approximation of underexpanded jet aerodynamics properties. Mean pressure is $\overline{P}_c = 6.67$ MPa. The adapted Mach number M_a is the exit Mach number for an adapted jet with the same generating pressure:

$$M_a^2 = \frac{2}{\gamma - 1}\left[\left(\frac{\overline{P}_c}{P_{atm}}\right)^{\frac{\gamma-1}{\gamma}} - 1\right] \tag{1}$$

In our case, the adapted exit Mach number M_a is 3.22. In the same way, an adapted jet equivalent diameter D_a can be

defined:

$$D_a^2/D^{*2} = \frac{1}{M_a}\left[\frac{2}{\gamma+1}(1+\frac{\gamma-1}{2}M_a^2)\right]^{\frac{\gamma+1}{2(\gamma-1)}} \tag{2}$$

which yields D_a/D_j=1.03.
The potential core of a jet is the zone downstream the nozzle exit where the flow derives from the pressure potential at the exit, and hence presents a constant velocity. It is usually assumed that the core region ends when the centerline velocity drops below 95% of the exhaust velocity. The length of the core region can be estimated through Nagamatsu & Horvay [7] experimental relation based on the exit Mach number:

$$L_c/D_j = 5.22M_j^{0.9} + 0.22 = 14.96 \tag{3}$$

Meanwhile, Eldred [8] explicited a relation based on the adapted Mach number and adapted nozzle diameter :

$$L_c/D_a = 3.45(1 + 0.38M_a)^2 = 17.06 \tag{4}$$

which leads to $L_c/D_j = 17.64$, which is longer. In this zone, a quasi-periodic shock cell pattern is visible. Shock cell length L_{shock} can be estimated with Tam & Tanna [9] relation:

$$L_{shock}/D_a = \frac{\Pi}{\mu_1}\sqrt{M_a^2 - 1} = 4.01 \tag{5}$$

where μ_1=2.4 is the first zero of the zero order Bessel function. Alternatively, $L_{shock}/D_j = 4.14$.

3. Numerical procedure

3.1 Computational domain

The computational domain is built from a simplified geometry of the experimental set-up. It features the combustion chamber aft end, the nozzle and a part of the motor external structure, as well as the ground. The plume develops in a semi-spherical propagative area which origin is the nozzle exit and radius extends further the first arc of transducers to $114D_j$. The area is truncated horizontally, to reproduce the reflective effects of the ground observed during the experiment, and the total volume is roughly 600 m^3. Global view and details of the domain are visible in Figure 5.

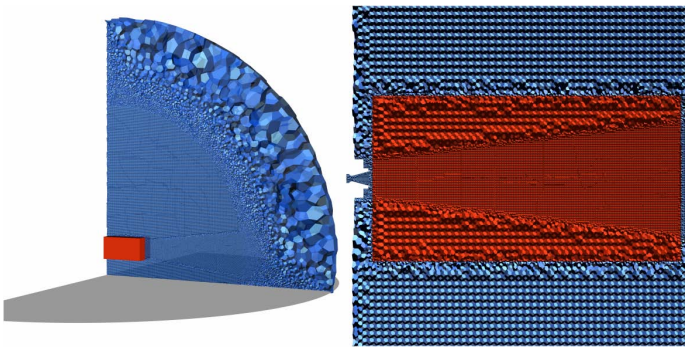

Figure 5: Grid view: *left:* global grid view and radiative user domain imbrication in orange, ground is grey; *right:* details of the radiative user domain and nozzle

Cedre allows computation on multiple user domains in which different physics may be solved. In order to avoid costly radiative computations, a small domain is extracted from the main domain. It is a cuboid of dimension $l \times h \times h$ (*c.f.* 2.2) that encloses the portion of plume visible by the IR camera. Navier-Stokes equations are resolved on both domains, but radiative computations are run on the small domain only with one-way coupling every 0.5 ms.

3.2 Grid

When computing LES simulations, the element size governs the highest bound of the computed turbulent eddies frequency range. The Smagorinsky sub grid scale model dissipates the eddies which frequency is above this bound. Jet noise has been thoroughly studied and the sources have been proved to be located in the jet [7, 10].

A refined zone is designed in the grid generation software that encloses the jet. It is a truncated cone beginning at nozzle exit which initial diameter is 2.57 D_j and final diameter is 20 D_j. Its length is 73 D_j, and aperture is 6.8° which agrees well with experimental measures from [11]. Cell diameter inside the zone is set to 7 mm.
In the propagative area, we focus on the IOP wave phenomenon. The experimental wave front is approximately $T = 1$ ms long [12] and propagates through a volume of uniform pressure and temperature at atmospheric conditions, yielding a characteristic wavelength of $\lambda = c \times T = 0.346$ m, c being the speed of sound at those conditions. Bogey and Bailly [13] showed that for low order space discretization scheme, 20 points per wavelength (PPW) must be used to ensure low dispersion and diffusion. Considering λ, the criterion leads to a maximum cell size of roughly $\Delta x = 0.346/20 = 17.3$ mm. This criterion must be matched by the grid on the wave path between sources and microphones. The domain further is coarsely grided to provide a buffer zone that will damp the acoutic waves before they reach the boundary.

Grid is generated with Star-ccm+ software. The cells are polyhedrons, that can be assimilated to spheres of diameter equal to Δx. In the considered domain, the resultant number of cells would be too large for the available ressources. Previous computations [12] carried out with Cedre showed that prior attention should be brought upon jet discretization before propagative area refinement. Thus the cell size is scaled up in this zone until cell number is in adequation with the ressources, with a final cell size $\Delta x = 30$ mm.

The final grid is composed of 23.5 M polyhedral elements which number of faces is represented in Figure 6. The

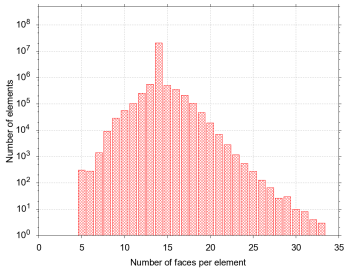

Figure 6: Computational grid elements ordered by number of faces

polyedrons are mainly 14-sided, and two of them present 34 faces. The total number of faces is 165 M.

3.3 Flow solver

The compressible flow solver Charme [14] resolves Navier-Stokes equations for the gas mixture. This latter is a mix of any number of possibly reacting species, with various thermodynamic state laws (perfect gas with variable heat capacities, tabulated real gas, compressible liquids...). Space discretization general framework is the cell-centered finite volume approach [15]. Interpolation follows a MUSCL type methodology, where space derivatives are evaluated algebraically from the neighbourhood of the cell, yielding to a polynomial reconstruction on each cell. These give two values at every point of the interface between two cells, which are used as input for the approximate Riemann solvers after limitation for monotony. These values are the basis for interface gradients and Navier-Stokes flux evaluation. Time integration proposed methods feature classical explicit Runge-Kutta methods as well as Euler implicit method.
Combustion products are composed of hot reducing species, that react with oxydizing ambient air when exiting the motor. Tsu and Brodwell [16] and Troyes and Vuillot [17] proved, with theoretical and numerical results respectively, that this after-burning phenomenon has a strong influence on IOP amplitude. Thus the computation must take into account the dominant species exiting the motor and the species from air, as well as intermediate species needed by the reactive scheme. This latter is a finite-rate chemistry scheme whose model implies seventeen reactions [18] and twelve species. To these species is added inert alumina, considered in a liquid state in the range of equilibrium temperatures considered (around 2300 K). Finally one gets: In order to avoid a very costly two phases computation, the dispersed

Table 1: Species transported

Dominant species (g)	Intermediate species (g)	Extra species (g)	Alumina (l)
H_2, O_2, H_2O, HCl, CO, CO_2	H, O, OH, Cl, Cl_2	N_2	Al_2O_3

phase of alumina is replaced by a gas of unknown thermodynamic properties (pink circle in Figure 7). The latter are set

so that the global thermodynamic properties of the particle-gas mix (yellow+drops in Figure) are identical to the global thermodynamic properties of the gaseous compounds plus the unknown gas mix (blue in Figure). In the computation,

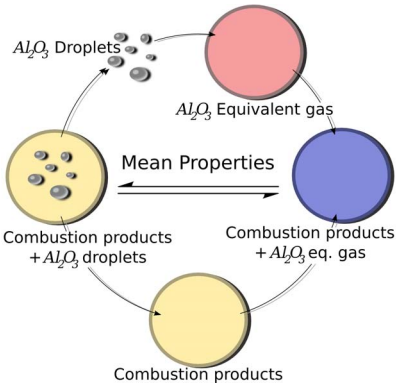

Figure 7: Equivalent gas procedure scheme

the specific heat capacities (C_p) are given by polynomial 7^{th} order functions of temperature (except for alumina which is constant).

3.4 Radiation solver

3.4.1 Presentation of the Astre solver

Astre [2, 19, 20, 21] is a radiative transfer solver based on a Monte Carlo method. This approach consists in following a finite large number of energy bundles (discrete amounts of energy, which can be thought of as a group of photons bound together) throughout their transport histories (from emission to absorption). Bundle characteristics (wavenumber, initial direction, emission point) and physical events (scattering, reflection off walls... except absorption) along bundle trajectories are chosen according to probability distributions by drawing random numbers. Absorption phenomenon is treated with pathlength method [22], also called "energy partionning" [23], which consists in computing exponential absorption along the path. Therefore, a bundle contributes to every cell it traverses. A bundle is traced until it either leaves the enclosure or until its energy is depleted below a given cutoff level. As all the bundles are statistically independent, the parallelization of Astre is realized by distributing the bundles over the cores.
As well as the conventional Forward Method (FM), different reciprocal methods, based on the exchange formulation of radiative transfer, are implemented in the Astre solver : ERM, ARM and ORM [3, 4, 22, 23]. In the case of the Emission Reciprocity Method (ERM), which has been carried out in the present work (*cf.* 3.4.3), the radiative powers (resp. radiative fluxes) are calculated only in the cells (resp. surface elements) which are source of optical path.

3.4.2 Adaptation of the Astre solver

The Astre solver has been initially developed in order to obtain radiative fluxes and powers integrated over the whole spectrum and all the directions. For the present application, the Astre solver has been adapted to reproduce experimental IR images in the spectral range 8 μm – 9.3 μm.
Experimental images have been numerically rebuilt by calculating radiative intensity from optical trajectories perpendicular to the camera surface. To obtain this result, bundles have been emitted only from surface elements constituting the boundary condition "camera". Initial direction of all the bundles has been systematically chosen perpendicular to the camera and theirs wavelengths have been chosen in the spectral range 8 μm – 9.3 μm. Then, the ERM method has been applied along bundle trajectories to compute radiative intensity from jet flow. Note that in this case, all the trajectories contribute to the intensity received by the camera. It would not be the case with the FM method or the other reciprocal methods. Indeed, due to scattering by particles, all the bundles, emitted by the medium in the direction perpendicular to the camera surface, would not reach the camera surface and would not contribute to the computing of the radiative intensity received by the camera.

3.4.3 Radiative property modelling

In the experimental spectral range, it has been assumed that only alumina particles, CO_2 and H_2O gaseous species contribute to the radiation received by the camera.

A Correlated-K model (CK) is used to compute absorption coefficients of CO_2 and H_2O gaseous species in the experimental spectral range 8 μm – 9,3 μm. The CK model parameters used have been generated by Soufiani and Taine [24] for radiation in the infrared spectral range (1-67 μm) and for atmospheric applications in the 300-2500 K temperature range.
For alumina droplets, Mie theory is assumed to calculate radiative properties (absorption and scattering coefficients and phase function). The complex refraction index m of alumina is modelled as a function of wavelength in accordance with the expression given by Joumani [25] such as:

$$m = 1.7 + ik(\lambda) \tag{6}$$

As the dispersed phase is replaced by an equivalent gas in the turbulent reactive flow calculation, the volume fraction of alumina particles is deduced from alumina mass fraction and the ratio between equivalent gas and alumina densities. Particles are considered at thermal equilibrium with the gases and a mean particle diameter is arbitrary fixed (*cf.* 4.3). However, a Gaussian function with a standard deviation equal to 10 % is considered to describe diameter particle distribution around this mean diameter.

3.5 Initial conditions

The whole domain is set to atmospheric temperature and pressure with air, modeling a seal at the combustion chamber aft-end.

3.6 Boundary conditions

Figure 8 is a schematic view of the computational domain boundaries.

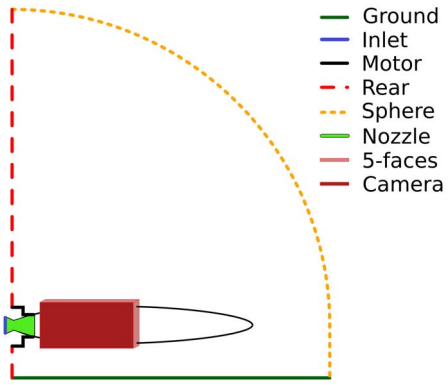

Figure 8: Boundaries schematic view

3.6.1 Gas solver

Limits “Ground”, “Motor” and “Nozzle” are no-slip adiabatic walls. The open-space limit “Rear” is a non-reflective updated boundary at atmospheric conditions, and “Sphere” is non-reflective non-updated outlet boundary at atmospheric conditions. “Inlet” boundary is treated by imposing total pressure, total temperature and uniform axial mass fraction injection of the considered chemical species. The total pressure fits the unsteady curve given by P_{far} experimental sensor from the seal break-up time t_0 to t_0+30 ms (*c.f.* 4), while composition of the combustion products and flow total temperature are computed from experimental combustion chamber pressure and propellant composition, using the in-house Onera thermodynamics equilibrium code Copelia.
Finally, the limits between the two user domains (“5-faces” and “Camera”) are treated as interface.

3.6.2 Radiation solver

Astre solver has specific boundary conditions. Both groups are treated as isothermal walls with a constant emissivity ε=1 (black body). Temperature is uniform and set to 500 K for “Camera” to numerically activate emission from this boundary towards the gases, as the ERM is employed, and set to 50 K for “5-faces” boundary, to ensure no emission from the boundary towards the camera plane.

3.7 Computation conditions

The spatial discretization is provided by a second order scheme and numerical Euler fluxes are always upwind (ODF). Time discretization is first order implicit and performed with a global time step. Implicit linear system resolution is done by a GMRES method with block diagonal preconditioning. Time step is set to 1.10^{-7} s. The cell size in the propagative zone associated with this time step ensures a low CFL number ($CFL << 1$).
Computations are carried out with CEDRE release 4.2 β. The fluid computation required 400,000 hours elapsed on 1024 Harpertown cores at CINES, and the IR post processing required 5 hours wall-time on 32 Nehalem cores at Onera.

4. Results

4.1 Instantaneous flow fields

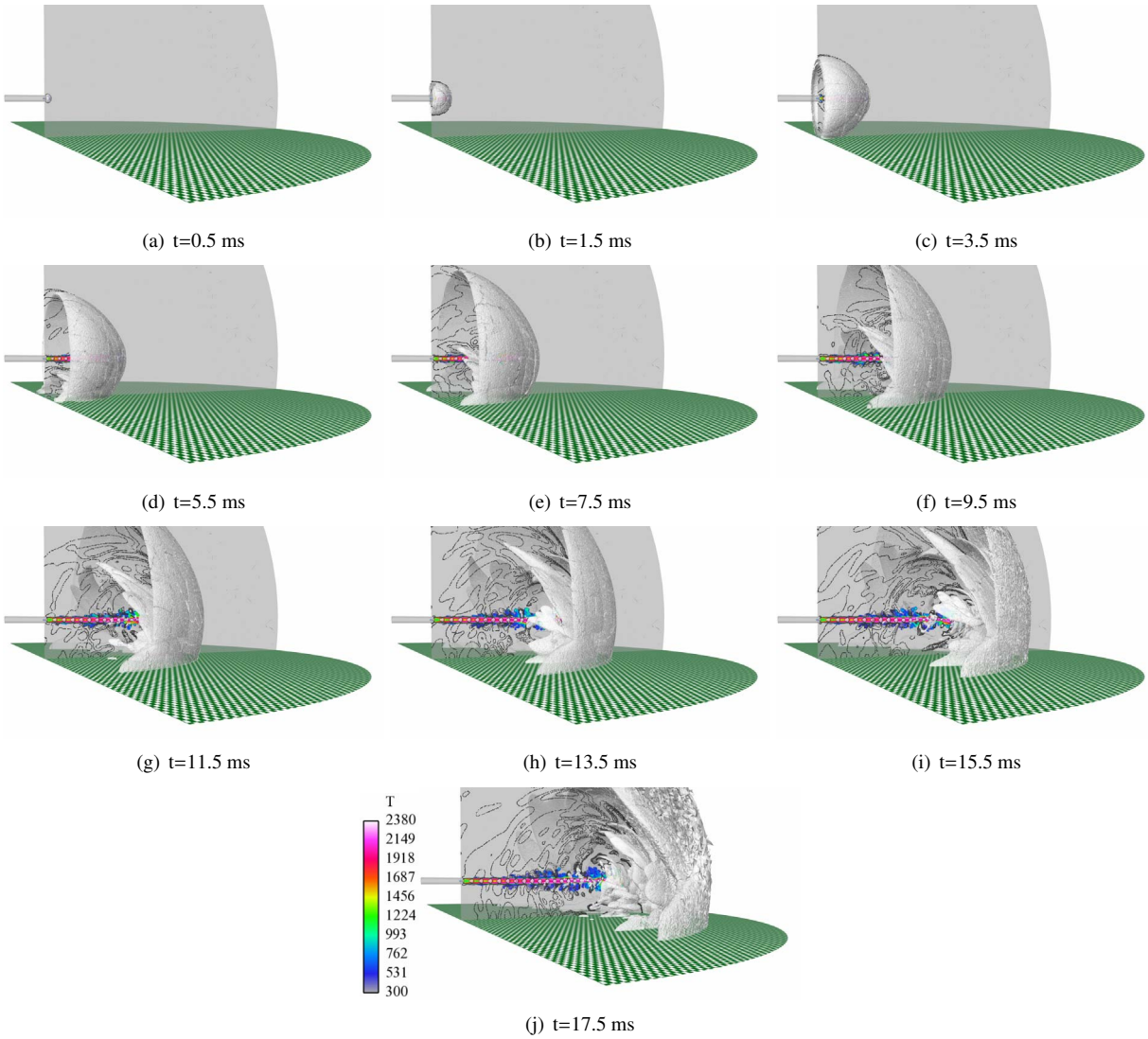

(a) t=0.5 ms (b) t=1.5 ms (c) t=3.5 ms

(d) t=5.5 ms (e) t=7.5 ms (f) t=9.5 ms

(g) t=11.5 ms (h) t=13.5 ms (i) t=15.5 ms

(j) t=17.5 ms

Figure 9: Temperature maps at plane x=0 from 300 K to 2380 K, 5 iso-contours of pressure from 101000 to 101600 Pa and iso-surface of pressure at 101825 Pa

On Figure 9, we can follow the interaction between the jet and the IOP, and between the IOP and the ground. At t=3.5 ms, the IOP reaches the ground, and reflexion begins. As the wave progresses, the jet extends, and finally the reflected wave has to cross the jet. A carefull observation shows that the jet splits the reflected wave in two. At first glance, the computed wave seems to be spherical. But at the t=3.5 ms, the jet seems to be pushing through the wave, and gives it a conical form.

Figure 10 is a time series of density maps on the x=0 plane. The IOP surpressure is visible in black, downstream

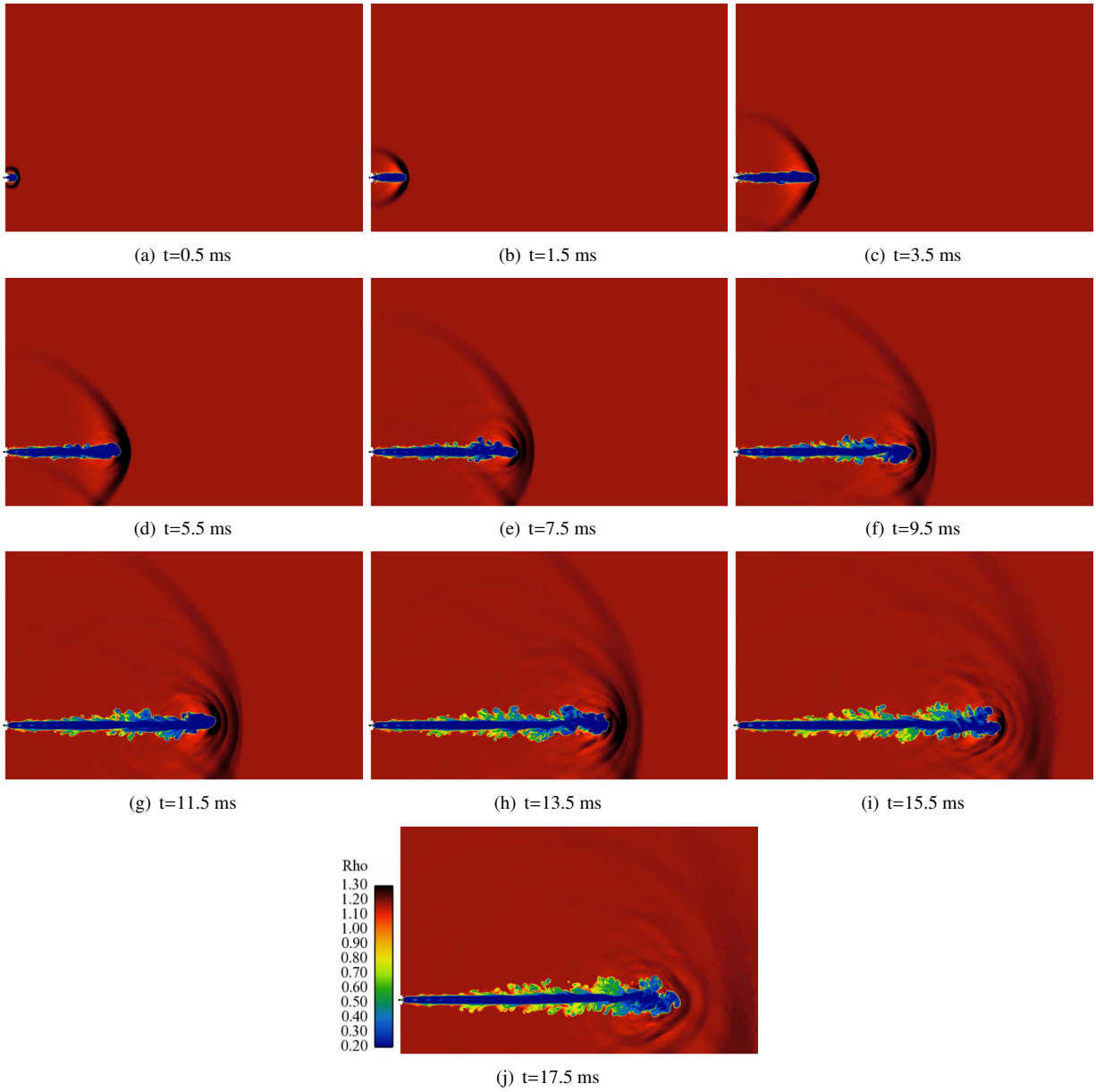

(a) t=0.5 ms (b) t=1.5 ms (c) t=3.5 ms

(d) t=5.5 ms (e) t=7.5 ms (f) t=9.5 ms

(g) t=11.5 ms (h) t=13.5 ms (i) t=15.5 ms

(j) t=17.5 ms

Figure 10: Density [kg.m^{-3}] map at x=0 plane

the jet. The ground is at the bottom of the image. The IOP reaches the ground at t=3.5 ms and reflection begins. The reflected wave is well visible later on. It reaches the jet around t=5.5 ms, and no trace of the reflected wave is visible above the jet later on. This confirms that the reflected IOP wave is absorbed by the jet in this plane: the jet splits the spherical wave in two. Moreover, the penetration of the low density jet inside the higher density IOP is well visible from start-up until t=5.5 ms. At t=7.5 ms, the jet has already fallen behind the wave.

4.2 Jet aerodynamics

A sampling of the jet centerline properties has been carried out every 0.5 ms. During the time period defined in 2.3, the extracted values of alumina mass fraction and axial velocity are averaged. In this time period, the core region proved to be steady.

The ratio of axial velocity along jet centerline axis over nozzle exit axial velocity is drawn on Figure 11. Determining the potential core length from this figure is difficult because of the successive shock cells. Therefore, as alumina is inert and only present in the jet, its mass fraction depends only on the jet mixing. Its mass fraction should be constant in the

potential core, and drop at then end of it. Figure 11 displays as well the mean alumina mass fraction at jet centerline over alumina mass fraction inside the combustion chamber. We consider the length of the potential core to be located at the downstream position where alumina mass fraction is below 95% of its value at nozzle exit, yielding x=14.92 D_j. It is between the values given by eq. 3 & 4. From the velocity curve, the first shock cell length can be determined and

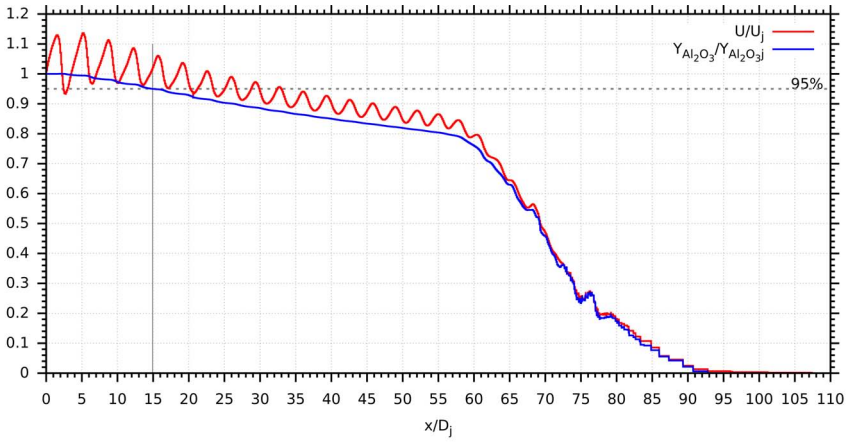

Figure 11: Mean jet axial velocity and mean alumina mass fraction at jet centerline

yields L_{shock}/D_j=3.61, which is smaller than the length predicted in eq. 5. These results confirm that the computed jet respects the main expected characteristics, and that the modelisation is adequate for IOP computation, which occurs at big scale. However, with the aim of jet noise computation, which mechanisms concern small scale eddies, the jet is clearly too stable. It is thought to be due to unsufficient mixing of the jet, probably because of a grid too coarse at the nozzle lips.

4.3 IR

We consider the droplet at thermal equilibrium with the surrounding gas, which is a strong hypothesis for big dropplets. Then, various computations were carried out with different droplet size ranging from 2.5 to 10 μm, which are a common size for solid propellant rocket, with no major effect on the solution. The alumina droplet size is arbitrarly fixed to 5 μm. Results at two key moments are displayed on Figure 12. At t=3.5 ms, a "fire ball" is observed on the visible and the

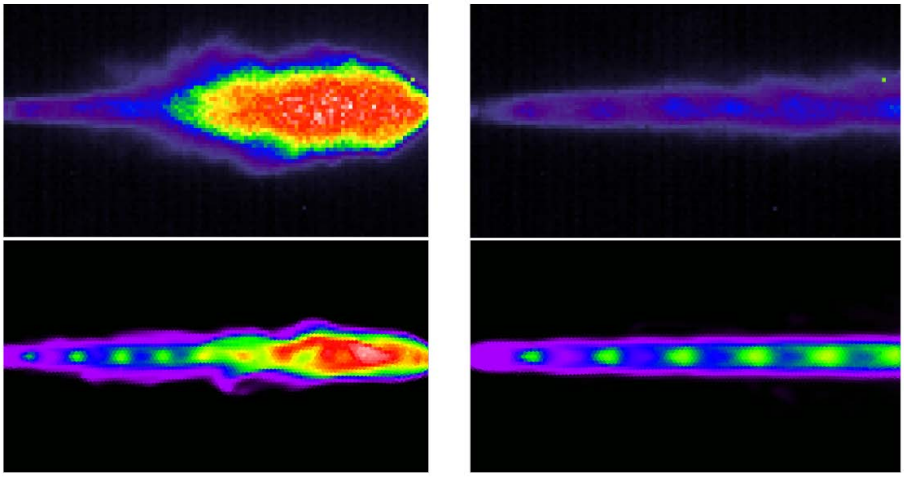

Figure 12: Comparison between recorded and computed IR fluxes. *Top:* recorded; *bottom:* computed; *left:* t=3.5 ms; *right:* t=15 ms

IR images. This hot spot convected downstream the jet is well reproduced by the computation. The length of the zones are comparable, even though the computed ball is narrower. Upstream of it, cell shocks are visible in the computation, as well as on the experimental image. Later, at t=15 ms, the shock cell structure of the jet is clearly visible. Both

images display 6 diamond-pattern shock cells, and the computation reproduces the location of cell number 1, 2, 3 and 6. Computed shock cells 4 and 5 are slightly downstream of the experiment.

4.4 Acoustical results

Figures 13.a) to 13.e) are the pressure histories recorded in the far-field on sensors C1 to C5. The beginning of the IOP wave is not clearly visible, as a first wave, issued from nozzle seal break-up, runs before it. However, this wave is well detached on the side sensors and is easily identified. The computed IOP is not well synchronized with the experiment

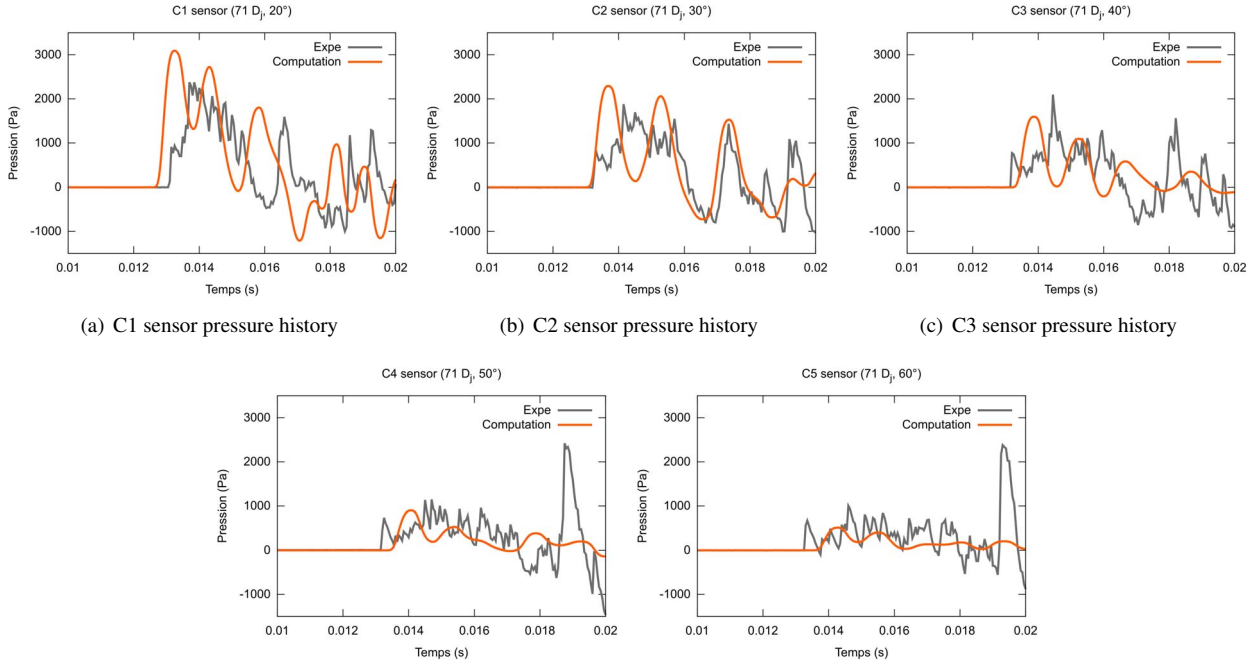

(a) C1 sensor pressure history (b) C2 sensor pressure history (c) C3 sensor pressure history

(d) C4 sensor pressure history (e) C5 sensor pressure history

Figure 13: Far-field sensors pressure histories

on the forward sensors. We think that it is due to the impact of the computed jet on the IOP that accelerates the wave at the jet centerline. However, levels are well reproduced as well as directivity, as can be seen on Figure 14. A maximum difference of 3 dB is found on microphone C5.

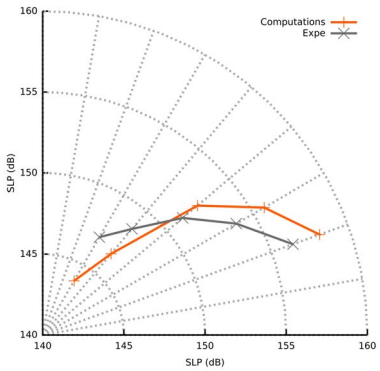

Figure 14: Directivity of the IOP waves

5. Conclusions

A Large Eddy Simulation has been carried out to identify the IOP phenomenon observed at a SRM ignition. This simulation took into account the various major species and the recombustion of the gaz with ambient air. IR emission of the jet has been performed to compare with recorded IR images. Numerical results proved to compare well with measured data: good agreement is found between the numerical and experimental levels of the IOP at the microphones, even though the computed wave is more directive. Moreover, time synchronization is quite good with microphones located at high angles, while forward angles sensors measure an IOP ahead of the experimental wave. This time shift is thought to be due to the impact of the jet on the wave during the first milliseconds. Finally, computed infrared emission compares well with experimental data. The "fire ball" phenomenon at start-up is well reproduced, and confirms the importance of recombustion. Jet aerodynamics at later time are validated by the good agreement between empirical caracterical values (potential core and shock cell length), and between IR plume signature (shock cell localisation). However, an exploration of the radiative solver boundary conditions influence must be performed to validate further the computation, as well as a more complete study of the alumina droplets size influence.
The grid refinement of the acoustic sources in the flow has a strong influence on the description of the IOP. The grid methodology for the IOP phenomena study is adequate, but is likely to need improvements (*e.g.* grid elements size at nozzle lips) for considering the small scale eddies responsible for jet noise.
Final understanding of IOP mechanisms is not achieved, and some concern points remain: separation of IOP and seal break-up generated wave is not visible in the computation, and may be reproduced for it participates in forward to the IOP amplitude (while being well separated at high angles). Finally, fine analysis of IOP wave front propagation structure may be done to characterize more precisely jet influence on IOP propagation.

6. Acknowledgements

This work was co-funded by CNES and ONERA in the framework of the R&T CNES Program. The authors would like to thank M. Prévost, P. Prévot, J. Varnier and G. Dunet from Onera in charge of the experiments used in this study. This work was granted access to the HPC resources of CINES under the allocation 2010-026497 made by GENCI (Grand Equipement National de Calcul Intensif).

References

[1] P. Chevalier, B. Courbet, D. Dutoya, P. Klotz, E. Ruiz, J. Troyes, and P. Villedieu, "Cedre: Development and validation of a multiphysic computational software," in *1st EUCASS*, (Moscow, Russia), 4-7 July 2005.

[2] L. Tessé, *Modélisation des transferts radiatifs dans les flammes turbulentes par une méthode de Monte Carlo*. PhD thesis, École Centrale Paris, 2001.

[3] L. Tessé, F. Dupoirieux, B. Zamuner, and J. Taine, "Radiative transfer in real gases using reciprocal and forward Monte Carlo methods and a Correlated-K approach," *International Journal of Heat and Mass Transfer*, vol. 45, pp. 2797–2814, 2002.

[4] F. Dupoirieux, L. Tessé, S. Avila, and J. Taine, "An optimized reciprocity Monte Carlo method for the calculation of radiative transfer in media of various optical thicknesses," *International Journal of Heat and Mass Transfer*, vol. 49, pp. 1310–1319, 2006.

[5] H. Ikawa and F. Laspesa, "Space shuttle SRM ignition overpressure prediction methodology," in *13th Plume Technology Meeting*, 1982.

[6] E. L. Morrisette and T. J. Goldberg, "Turbulent-flow separation criteria for overexpanded supersonic nozzles," Tech. Rep. 1207, NASA, Langley Research Center, 1978.

[7] H. T. Nagamatsu and G. Horvay, "Supersonic jet noise," in *AIAA 8th aerospace sciences meeting*, 1970.

[8] K. M. Eldred and al., "Acoustic loads generated by the propulsion system," Tech. Rep. SP-8072, NASA, 1971.

[9] C. K. W. Tam and H. K. Tanna, "Shock associated noise of supersonic jets from convergent-divergent nozzles," *journal of sound and vibration*, vol. 81, pp. 337–358, 1982.

[10] H. K. Tanna, "An experimental study of jet noise. Part I : Turbulent mixing noise.," *Journal of Sound and Vibrations*, vol. 50, pp. 403–428, 1977.

[11] S. C. Koria and K. W. Lange, "An experimental study on the behaviour of an underexpanded supersonic gas jet," *Arch. Eisenhüttenwes. 55*, vol. 9, pp. 427–432, 1984.

[12] J. Dargaud, J. Troyes, and F. Vuillot, "Numerical simulation of model solid rocket motor ignition overpressure waves. Part I : Horizontal free jet with reflective ground," in *17th International Conference on Sound and Vibration*, (Cairo), 2010.

[13] C. Bogey and C. Bailly, "A family of low dispersive and low dissipative explicit schemes for flow and noise computations," *Journal of Computational Physics*, vol. 194, pp. 194–214, 2004.

[14] A. Refloch, B. Courbet, A. Murrone, P. Villedieu, C. Laurent, P. Gilbank, J. Troyes, L. Tessé, G. Chaineray, J. Dargaud, E. Quémerais, and F. Vuillot, "CEDRE software," *Aerospace Lab*, vol. 2, 2011.

[15] B. Courbet, C. Benoit, V. Couaillier, F. Haider, M. Le Pape, and S. Péron, "Space discretization methods," *Aerospace Lab*, vol. 2, 2011.

[16] J. E. Broadwell and C. N. Tsu, "Transient pressures caused by rocket start and shutdown in ducted launchers," *Journal of spacecraft and rockets*, vol. 4, pp. 1323–1328, 1967.

[17] J. Troyes and F. Vuillot, "Numerical simulations of a model solid rocket motor ignition overpressure wave," in *44th AIAA/ASME/SAE/ASEE Joint Propulsion Conference*, (Hartford, CT), 21-23 July 2008. AIAA-2008-5133.

[18] J. Troyes, I. Dubois, V. Borie, and A. Boischot, "Multi-phase reactive numerical simulations of a model solid rocket motor exhaust jet," in *42nd AIAA/ASME/SAE/ASEE Joint Propulsion Conference and Exhibit*, (Sacramento, CA), 9-12 July 2006. AIAA 2006-4414.

[19] L. Tessé and J.-M. Lamet, "Radiative transfer modeling developed at Onera for numerical simulations of reactive flows," *Aerospace Lab*, vol. 2, 2011.

[20] L. Tessé, F. Dupoirieux, and J. Taine, "Monte Carlo modeling of radiative transfer in a turbulent sooty flame," *International Journal of Heat and Mass Transfer*, vol. 47, pp. 555–572, 2004.

[21] L. Tessé, S. Avila, F. Dupoirieux, and J. Taine, "Coupled modeling of aerothermochemistry: Soot formation and radiation in a turbulent diffusion flame," in *13th International Heat Transfer Conference*, (Sydney, Australia), 2006.

[22] J. T. Farmer and J. R. Howell, "Monte Carlo strategies for radiative transfer in participating media," *Advances in Heat Transfer*, vol. 31, pp. 1–97, 1998.

[23] M. F. Modest, *Radiative Heat Transfer*. Academic Press, 2003.

[24] A. Soufiani and J. Taine, "High temperature gas radiative property parameters of statistical narrow-band model for H_2O, CO_2 and CO, and Correlated-K model for H_2O and CO_2," *International Journal of Heat and Mass Transfer*, vol. 40, pp. 987–991, 1997.

[25] Y. Joumani, *Transferts radiatifs dans les moteurs à propergol solide*. PhD thesis, Université de Valenciennes et du Hainaut Cambresis, 2001.